Bull Volcanol (2005) 67:129–143
DOI 10.1007/s00445-004-0367-5

RESEARCH ARTICLE

Steven L. Quane · James K. Russell

Ranking welding intensity in pyroclastic deposits

Received: 11 August 2003 / Accepted: 19 May 2004 / Published online: 7 July 2004

Abstract Welding of pyroclastic deposits involves flattening of glassy pyroclasts under a compactional load at temperatures above the glass transition temperature. Progressive welding is recorded by changes in the petrographic (e.g., fabric) and physical (e.g., density) properties of the deposits. Mapping the intensity of welding can be integral to studies of pyroclastic deposits, but making systematic comparisons between deposits can be problematical. Here we develop a scheme for ranking welding intensity in pyroclastic deposits on the basis of petrographic textural observations (e.g., oblateness of pumice lapilli and micro-fabric orientation) and measurements of physical properties, including density, porosity, point load strength and uniaxial compressive strength. Our dataset comprises measurements on 100 samples collected from a single cooling unit of the Bandelier Tuff and parallel measurements on 8 samples of more densely welded deposits. The proposed classification comprises six ranks of welding intensity ranging from unconsolidated (Rank I) to obsidian-like vitrophyre (Rank VI) and should allow for reproducible mapping of subtle variations in welding intensity between different deposits. The application of the ranking scheme is demonstrated by using published physical property data on welded pyroclastic deposits to map the total accumulated strain and to reconstruct their pre-welding thicknesses.

Keywords Welding · Ignimbrite · Pyroclastic · Metrics · Rank · Bandelier Tuff · Physical properties · Strain

Editorial Responsibility: T. Druitt

S. L. Quane · J. K. Russell (✉)
Igneous Petrology Laboratory, Earth and Ocean Sciences,
The University of British Columbia,
6339 Stores Rd., V6T 1Z4 Vancouver, B.C.
e-mail: krussell@eos.ubc.ca
Tel.: +1-604-8222703
Fax: +1-604-8226088

Introduction

The welding process involves sintering, compaction and flattening of hot glassy pyroclastic material (e.g., Smith 1960a; Ross and Smith 1961; Cas and Wright 1987). Pronounced changes in physical properties attend welding; as welding intensifies, for example, primary porosity is reduced, density increases (e.g., Ragan and Sheridan 1972; Streck and Grunder 1995; Rust and Russell 2000) and the deposit becomes progressively more foliated (e.g., Smith 1960a; Ragan and Sheridan 1972; Sheridan and Ragan 1976; Peterson 1979). For most pyroclastic deposits, especially those resulting from en masse deposition (e.g., Sparks 1976; Sheridan and Ragan 1976; Wright and Walker 1981), the strain due to welding accumulates immediately after deposition (e.g., Smith 1960a; Ross and Smith 1961; Quane et al. 2004). In such cases, the intensity of welding reflects the aggregate effects of the load of the overlying column and time of residence at temperatures above the material's glass transition temperature (Tg) (Riehle et al. 1995; Giordano et al. 2000; Russell and Quane 2004). The welding intensity reflects the volume strain resulting from porosity loss during compaction and, therefore, varies systematically with stratigraphic position (e.g., depth and lateral distance). However in deposits resulting from high-temperature progressive aggradation, much of the agglutination and compaction of glassy particles may actually occur during emplacement (e.g., Branney and Kokelaar 1992; Sumner and Branney 2002). The resulting "high-grade" ignimbrites are highly-agglutinated and lava-like in character and typically do not exhibit systematic variations in welding intensity (e.g., Kobberger and Schmincke 1999; Sumner and Branney 2002). In fact, these deposits commonly host textures and features consistent with rheomorphic flow (Schmincke and Swanson 1967; Walker and Swanson 1968; Wolff and Wright 1981; Branney and Kokelaar 1992; Kobberger and Schmincke 1999; Sumner and Branney 2002) representing a non-coaxial strain that is not dependent on porosity loss (e.g., pure or sim-

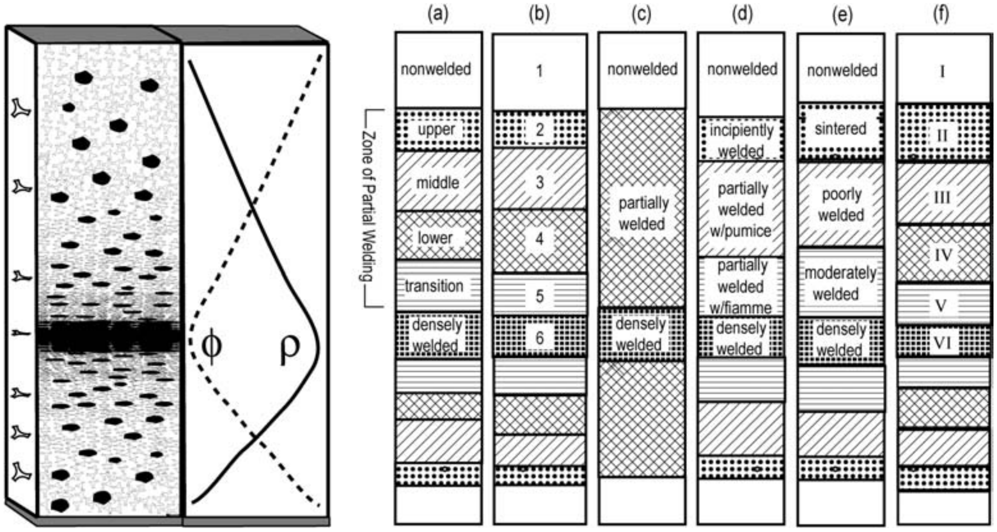

Fig. 1a–f Previous schemes for classifying zones of equal welding intensity in a single cooling unit of ash flow tuff based on changes in physical properties (e.g., ρ, ϕ) and shard shape. Schematic column on left represents textural variations in ash shards (open) and pumice lapilli (solid) as well as typical variations in ρ and ϕ. Schematic columns a–f represent schemes for defining welding intensity present in the literature: **a**) Smith (1960b; petrographic observations on Bandelier Tuff), **b**) Smith and Bailey (1966; porosity of Bandelier Tuff), **c**) Sheridan and Ragan (1976; density of Bishop Tuff) and Peterson (1979; fiamme elongation of Apache Leaf Tuff), **d**) Streck and Grunder (1995; density of Rattlesnake Tuff), **e**) Wilson and Hildreth (2003; density of Bishop Tuff), **f**) This study

ple shear; Sheridan and Ragan 1976; Kobberger and Schmincke 1999; Quane et al. 2004).

Welded pyroclastic flow deposits can serve as excellent stratigraphic markers (e.g., Smith and Bailey 1966) and mapping distributions in welding intensity has been used for a variety of purposes. Streck and Grunder (1995) used spatial variations in welding facies to constrain aerial extent and eruptive volume of the Rattlesnake Tuff. Profiles of welding intensity in pyroclastic deposits have also been used to estimate pre-welding thicknesses (e.g., Sheridan and Ragan 1976), displacements across faults (e.g., Peterson 1979), hydrologic variability in tuffs for waste disposal assessment (e.g., Istok et al. 1994), and variations in rock strength for engineering applications (e.g., Price and Bauer 1985). There is, however, no agreed upon standard means of recording welding intensity and this limits comparisons within and between welded pyroclastic deposits. Unit 4 of the Tshirege member of the Bandelier Tuff has been characterized by many workers and serves as an example (e.g., Smith and Bailey 1966; Vaniman and Wohletz 1990, 1991; Goff 1995). The unit is interpreted to represent a single cooling unit of ignimbrite and has a base clearly defined by a sandy surge deposit (Krier et al. 1998). Welding variations in the same section of the deposit have been described, by different workers, as nonwelded to partially welded (Broxton and Reneau 1995) or as nonwelded to densely welded (Krier et al. 1998). Each study is internally consistent but appears to describe different ranges in welding intensity.

The purpose of this paper is three-fold. Firstly, we review the past practices used to map welding facies. Secondly, we present physical property measurements on samples of welded pyroclastic deposits including: porosity (ϕ), density (ρ), point load strength (PLST), uniaxial compressive strength (UCS), pumice lapilli oblateness and micro-fabric orientation. The physical properties are evaluated as metrics of total strain and welding intensity. We conclude with a classification system comprising six indices for ranking the intensity of welding in pyroclastic deposits. These indices have the attributes that they: (1) are explicitly tied to deformation-induced textural changes which makes the system useful in the field, (2) reconcile the terminology and divisions for welding intensity developed previously (e.g., Smith 1960b; Streck and Grunder 1995; Wilson and Hildreth 2003), and (3) should provide a consistent framework for semi-quantitative mapping of welding facies in pyroclastic deposits.

Previous work

Semi-quantitative schemes used to describe welding intensity are summarized in Fig. 1 (Smith 1960b; Smith and Bailey 1966; Sheridan and Ragan 1976; Peterson 1979; Streck and Grunder 1995; Wilson and Hildreth 2003). Smith (1960b) proposed six zones of welding based on petrographic traits of lapilli and ash sized fragments (Fig. 1a). Smith and Bailey (1966) created six zones based on the range of estimated porosities in multiple sections of Bandelier Tuff (Fig. 1b). Sheridan and Ragan (1976) and Peterson (1979) used measurements of bulk density and pumice flattening ratios, respectively, to identify three grades of welding for the Bishop Tuff and Apache Leaf Tuff, respectively (Fig. 1c). Streck and Grunder (1995) developed the most complete scheme; they distinguished five zones based on measurements of bulk density and petrographic features of the Rattlesnake Tuff (Fig. 1d). Similarly, Wilson and Hildreth (2003) used field characteristics and measurements of density to create a scheme comprising five zones of welding intensity for the Bishop Tuff (Fig. 1e).

The schemes described above use petrographic observations and/or a number of physical properties to define their welding ranks. However, the relative effectiveness of each physical property (or metric) to track welding variations is poorly known, as are the covariances between the individual metrics.

Metrics of welding intensity

We present measurements of ρ, ϕ, point load strength (PLST), uniaxial compressive strength (UCS), oblateness and fabric angle for samples of Bandelier Tuff, New Mexico (e.g., Smith and Bailey 1966; Table 1; Fig. 2). The suite includes 100 samples collected at a depth spacing of <1 m from 4 drill cores (SCC-1, SCC-2, SCC-4 and NISC-2) of Unit 4 in the Tshirege member of the Bandelier Tuff (Broxton and Reneau 1995) spaced within ~100 m. At this location, Unit 4 is a ~20-m-thick unit with a base defined by the presence of a crystal-rich, sandy surge deposit (Krier et al. 1998). These data (Table 1) are supplemented by measurements from eight samples of more densely welded material collected from the Devine Canyon Tuff and Walcott Tuff (Table 2). The highest degree of secondary crystallization exhibited by any of the samples investigated here is equivalent to the cryptocrystalline vapor phase zone of Streck and Grunder (1995), in which, the material maintains its vitroclastic texture but shows axiolitic growth of recrystallized cristobalite. This limited style of secondary crystallization is assumed to have negligible effects on the physical property measurements. Wilson and Hildreth (2003), for example, showed that the density of Bishop Tuff samples was unaffected by minor devitrification and vapor phase alteration. However as the extent of devitrification and vapor phase alteration increases, vitroclastic textures will tend to be completely replaced and the physical properties will be strongly impacted.

Density and porosity

Density and porosity vary systematically in all four sections of the Bandelier Tuff and define maxima and minima, respectively, at a depth of between 13 and 17 m (Fig. 2; Table 1). Bulk densities for all 108 samples were determined using the hydrostatic weighing technique at 25°C. Core or hand samples having a bulk volume of at least 150 cm^3 were rendered impermeable to H_2O by spraying them with a negligible volume and weight of Krylon® Crystal Clear aerosol coating. Densities (ρ_T) were calculated from:

$$\rho_T = \rho_f[W_1/(W_1 - W_2)] \tag{1}$$

where ρ_f is the density of the fluid, W_1 is the weight of the samples in air and W_2 is the weight of the sample immersed in H_2O. Specific details on the procedure can be found in Hutchison (1974) and Muller (1977). Accuracy of the technique was established by measurements of multiple samples of pure quartz (±0.01 g/cm^3). An estimate of analytical precision was determined by replicate measurements on two samples (1σ ~ <1%).

Sample porosity was measured by helium pycnometry. Samples were weighed and then flooded with helium to determine the volume of framework material (i.e., the skeletal volume). This technique measures skeletal density (ρ_s) if all porosity is connected and total porosity (ϕ_T) is then calculated from:

$$\phi_T = \frac{\rho_S - \rho_T}{\rho_s} \tag{2}$$

where ρ_T is the bulk density of the sample. If all the pores are connected, then ϕ_T is a true estimate of sample porosity. To test for unconnected (isolated) porosity, samples were powdered and matrix density was determined by He pycnometry (e.g., Rust et al. 1999). These ancillary measurements showed that, for the complete spectrum of samples of Bandelier Tuff, all porosity is connected. Experimental uncertainties (1σ) are estimated to be ~1% relative.

Rock strength

Rock strength as measured by point load strength (*PLST*) and unconfined or uniaxial compressive strength (*UCS*) offers an alternate, albeit indirect, measure of welding intensity. These measurements also define a maximum at depths between 14 and 17 m (Fig. 2). *PLST* measures the tensile strength of a rock specimen by application of a vertical load (perpendicular to the fabric) until the sample fails (i.e., Quane and Russell 2003). *PLST* measurements were made on 41 samples from 2 of the drill cores of Bandelier Tuff (SCC-1 and SCC-4; Fig. 2) and all values are reported after scaling to a common size and geometry (e.g., 50 mm core diameter). The relative precision (1σ) of the measurement is ~10% (e.g., Quane and Russell 2003).

UCS determines the true breaking strength of a material under axial loading. Measurements were performed on right circular cylinders with a length (L) at least 2 times the width (W) having a minimum diameter (D) of 50 mm. Reported *UCS* values are the mean of the peak load at failure from multiple measurements (~5) from each sample and average standard deviation (1σ) is approximately 15%. *UCS* measurements are more representative of the true strength of material but are much more expensive in time and resources, thus, we made *UCS* measurements only on a subset of samples (Table 1). However, *UCS* can also be predicted from measured values of *PLST* (Quane and Russell 2003) using the equation:

$$UCS = 3.86 \cdot PLST^2 + 5.65 \cdot PLST \tag{3}$$

Table 1 Physical property data collected from four drill cores in Unit 4 of the Tshirege member of the Bandelier tuff including density (ρ), porosity (ϕ), point load strength (*PLST*), uniaxial compressive strength (*UCS*), fabric angle (FA) and oblateness (OB)

Sample	Depth (m)	ρ (g/cm^3)	2σ	ϕ	2σ	*PLST* (MPa)	1σ	*UCS* (MPa)	1σ	FA	1σ	OB	1σ
SCC1–1	0.00	1.27	0.002	0.51	0.006	0.23	0.06	–	–	46.90	6.43	0.40	0.03
SCC1–2	1.30	1.32	0.002	0.49	0.006	0.23	0.03	2.07	0.56	39.15	5.46	0.42	0.05
SCC1–3	2.36	1.34	0.002	0.49	0.006	0.19	0.02	–	–	39.60	5.38	0.42	0.04
SCC1–4	3.51	1.36	0.002	0.48	0.006	0.19	0.04	2.44	–	31.32	4.55	0.44	0.04
SCC1–5	3.89	1.38	0.002	0.47	0.006	0.27	0.03	2.37	0.53	38.65	5.42	0.54	0.03
SCC1–6	4.73	1.40	0.002	0.46	0.006	0.31	0.05	–	0.10	37.35	5.14	0.52	0.04
SCC1–7	5.64	1.44	0.002	0.45	0.005	0.39	0.08	2.38	–	34.54	5.14	0.51	0.05
SCC1–8	6.55	1.45	0.003	0.45	0.005	0.40	0.03	3.27	0.35	32.99	4.80	0.55	0.03
SCC1–9	7.62	1.50	0.003	0.43	0.005	0.58	0.06	4.26	0.23	33.81	4.80	0.57	0.04
SCC1–10	8.23	1.52	0.003	0.42	0.005	0.54	0.08	5.34	0.46	–	–	0.59	0.04
SCC1–11	8.99	1.53	0.003	0.41	0.005	0.54	0.03	–	–	36.49	5.23	0.58	0.03
SCC1–12	9.91	1.57	0.003	0.39	0.005	0.77	0.10	–	–	30.31	4.62	0.58	0.04
SCC1–13	11.81	1.59	0.003	0.39	0.005	0.58	0.02	–	–	32.29	4.83	0.61	0.06
SCC1–14	12.42	1.64	0.003	0.36	0.004	0.78	0.08	6.74	0.39	31.11	4.59	0.60	0.05
SCC1–15	13.57	1.70	0.003	0.34	0.004	0.91	0.02	–	–	22.02	3.46	0.68	0.05
SCC1–16	16.92	1.80	0.003	0.30	0.004	1.61	0.03	12.78	3.13	22.54	3.53	0.69	0.04
SCC1–17	17.45	1.78	0.003	0.31	0.004	1.40	0.05	12.41	1.31	25.29	4.11	0.65	0.03
SCC1–18	18.06	1.72	0.003	0.33	0.004	1.39	0.11	–	–	32.19	4.68	0.64	0.03
SCC1–19	18.75	1.60	0.003	0.38	0.005	0.82	0.08	–	–	29.37	4.38	0.62	0.02
SCC1–20	19.44	1.59	0.00	0.38	0.005	0.56	0.04	–	–	28.74	4.35	0.45	0.04
SCC2–1	0.00	1.28	0.002	0.51	0.006	–	–	–	–	–	–	0.40	0.06
SCC2–2	0.46	1.28	0.002	0.52	0.006	–	–	–	–	–	–	0.41	0.05
SCC2–3	1.22	1.33	0.002	0.5	0.006	–	–	–	–	–	–	0.39	0.04
SCC2–4	1.98	1.36	0.002	0.48	0.006	–	–	–	–	–	–	0.47	0.06
SCC2–5	3.43	1.36	0.002	0.48	0.006	–	–	–	–	–	–	0.55	0.03
SCC2–6	4.42	1.40	0.002	0.47	0.006	–	–	–	–	–	–	–	–
SCC2–7	5.18	1.43	0.002	0.45	0.005	–	–	–	–	–	–	0.55	0.05
SCC2–8	6.40	1.45	0.003	0.45	0.005	–	–	–	–	–	–	0.53	0.05
SCC2–9	7.70	1.52	0.003	0.4	0.005	–	–	–	–	–	–	0.62	0.04
SCC2–10	9.07	1.63	0.003	0.38	0.005	–	–	–	–	–	–	0.60	0.03
SCC2–11	10.37	1.63	0.003	0.38	0.005	–	–	–	–	–	–	0.60	0.03
SCC2–12	11.81	1.65	0.003	0.36	0.004	–	–	–	–	–	–	0.65	0.04
SCC2–13	12.84	1.72	0.003	0.35	0.004	–	–	–	–	–	–	–	–
SCC2–14	13.57	1.77	0.003	0.32	0.004	–	–	–	–	–	–	0.70	0.03
SCC2–15	14.33	1.82	0.003	0.32	0.004	–	–	–	–	–	–	–	–
SCC2–16	14.94	1.84	0.003	0.3	0.004	–	–	–	–	–	–	0.77	0.02
SCC2–17	15.63	1.84	0.003	0.29	0.004	–	–	–	–	–	–	0.73	0.04
SCC2–18	16.54	1.77	0.003	0.32	0.004	–	–	–	–	–	–	0.63	0.05
SCC2–19	18.06	1.43	0.002	0.45	0.005	–	–	–	–	–	–	–	–
SCC2–20	19.28	1.45	0.003	0.45	0.005	–	–	–	–	–	–	–	–
SCC4–1	0.00	1.41	0.002	0.46	0.006	0.66	0.07	–	–	–	–	0.38	0.04
SCC4–2	0.38	–	–	–	–	–	–	–	–	–	–	–	–
SCC4–3	1.68	1.31	0.002	0.5	0.006	0.19	0.01	–	–	–	–	0.51	0.03
SCC4–4	2.59	1.35	0.002	0.48	0.006	–	–	–	–	–	–	–	–
SCC4–5	3.51	1.40	0.002	0.46	0.006	0.24	0.01	–	–	–	–	0.45	0.08
SCC4–6	3.89	1.41	0.002	0.46	0.006	–	–	–	–	–	–	–	–
SCC4–7	4.42	1.42	0.002	0.45	0.005	0.35	0.04	–	–	–	–	0.48	0.04
SCC4–8	4.95	1.41	0.002	0.46	0.005	–	–	–	–	–	–	–	–
SCC4–9	5.95	1.49	0.003	0.43	0.005	0.30	0.05	–	–	–	–	0.56	0.04
SCC4–10	6.40	1.49	0.003	0.43	0.005	0.33	0.05	–	–	–	–	0.52	0.04
SCC4–11	7.09	1.49	0.003	0.42	0.005	0.26	0.05	–	–	–	–	0.56	0.04
SCC4–12	8.23	1.58	0.003	0.4	0.005	0.39	0.08	–	–	–	–	0.61	0.02
SCC4–13	8.77	1.59	0.003	0.39	0.005	0.72	0.07	–	–	–	–	0.63	0.03
SCC4–14	9.45	1.59	0.003	0.39	0.005	–	–	–	–	–	–	–	–
SCC4–15	10.02	1.63	0.003	0.37	0.004	0.70	0.08	–	–	–	–	0.63	0.04
SCC4–16	10.52	1.61	0.003	0.39	0.005	0.70	0.07	–	–	–	–	0.64	0.03
SCC4–17	11.39	1.67	0.003	0.36	0.004	0.61	0.18	–	–	–	–	0.67	0.03
SCC4–18	11.93	1.71	0.003	0.34	0.004	0.73	0.1	–	–	–	–	0.61	0.05
SCC4–19	12.65	1.76	0.003	0.32	0.004	0.87	0.2	–	–	–	–	0.69	0.03
SCC4–20	13.26	1.79	0.003	0.32	0.004	0.92	0.12	–	–	–	–	0.69	0.03
SCC4–21	13.87	1.78	0.003	0.31	0.004	1.01	0.14	–	–	–	–	0.70	0.02
SCC4–22	14.63	1.68	0.003	0.36	0.004	0.86	0.11	–	–	–	–	0.62	0.03
SCC4–23	15.09	1.63	0.003	0.37	0.004	0.80	0.08	–	–	–	–	0.60	0.03
SCC4–24	15.85	1.59	0.003	0.39	0.005	0.31	0.01	–	–	–	–	0.62	0.04
SCC4–25	16.46	1.45	0.003	0.44	0.005	0.25	0.06	–	–	–	–	0.62	0.05
SCC4–26	16.92	1.42	0.002	0.46	0.006	0.09	0.02	–		–	–	0.49	0.04
SCC4–27	18.06	1.33	0.002	0.5	0.006	–	–	–	–	–	–	–	–

Table 1 (continued)

Sample	Depth (m)	ρ (g/cm^3)	2σ	ϕ	2σ	*PLST* (MPa)	1σ	*UCS* (MPa)	1σ	FA	1σ	OB	1σ
SCC4–28	18.67	1.36	0.002	0.48	0.006	–	–	–	–	–	–	–	–
NISC2–1	0.00	1.23	0.002	0.52	0.006	–	–	–	–	–	–	0.36	0.05
NISC2–2	0.23	1.23	0.002	0.53	0.006	–	–	–	–	–	–	0.40	0.07
NISC2–3	1.37	1.28	0.002	0.52	0.006	–	–	–	–	–	–	0.50	0.05
NISC2–4	1.75	1.31	0.002	0.48	0.006	–	–	–	–	–	–	–	–
NISC2–5	2.44	1.33	0.002	0.48	0.006	–	–	–	–	–	–	0.50	0.05
NISC2–6	3.05	1.36	0.002	0.47	0.006	–	–	–	–	–	–	0.49	0.04
NISC2–7	3.43	1.38	0.002	0.46	0.006	–	–	–	–	–	–	–	–
NISC2–8	3.96	1.38	0.002	0.46	0.006	–	–	–	–	–	–	0.59	0.04
NISC2–9	4.65	1.40	0.002	0.45	0.005	–	–	–	–	–	–	0.60	0.04
NISC2–10	4.99	1.43	0.002	0.44	0.005	–	–	–	–	–	–	0.58	0.04
NISC2–11	5.49	1.46	0.003	0.43	0.005	–	–	–	–	–	–	0.62	0.03
NISC2–12	6.17	1.46	0.003	0.44	0.005	–	–	–	–	–	–	0.59	0.05
NISC2–13	6.63	1.49	0.003	0.43	0.005	–	–	–	–	–	–	–	–
NISC2–14	7.09	1.55	0.003	0.4	0.005	–	–	–	–	–	–	0.68	0.03
NISC2–15	7.47	1.51	0.003	0.41	0.005	–	–	–	–	–	–	0.67	0.02
NISC2–16	8.08	1.55	0.003	0.4	0.005	–	–	–	–	–	–	–	–
NISC2–17	8.69	1.56	0.003	0.4	0.005	–	–	–	–	–	–	0.62	0.03
NISC2–18	9.26	1.58	0.003	0.39	0.005	–	–	–	–	–	–	–	–
NISC2–19	9.60	1.60	0.003	0.38	0.005	–	–	–	–	–	–	–	–
NISC2–20	10.14	1.59	0.003	0.39	0.005	–	–	–	–	–	–	0.67	0.03
NISC2–21	10.90	1.62	0.003	0.37	0.004	–	–	–	–	–	–	–	–
NISC2–22	11.66	1.66	0.003	0.36	0.004	–	–	–	–	–	–	0.71	0.03
NISC2–23	12.42	1.71	0.003	0.34	0.004	–	–	–	–	–	–	–	–
NISC2–24	13.11	1.71	0.003	0.33	0.004	–	–	–	–	–	–	0.72	0.01
NISC2–25	13.95	1.68	0.003	0.35	0.004	–	–	–	–	–	–	–	–
NISC2–26	14.71	1.63	0.003	0.37	0.004	–		–	–	–	–	–	–
NISC2–27	15.40	1.55	0.003	0.4	0.005	–	–	–	–	–	–	0.64	0.03
NISC2–28	16.16	1.48	0.003	0.43	0.005	–	–	–	–	–	–	0.49	0.05
NISC2–29	17.38	1.38	0.002	0.47	0.006	–	–	–	–	–	–	–	–
NISC2–32	19.89	1.30	0.002	0.5	0.006	–	–	–	–	–	–	–	–

Petrographic features

Welding deformation is manifest by measurable variations in the petrographic features oblateness and fabric angle. Oblateness increases to a maximum and fabric angle decreases to a minimum between 13 and 17 m depth in measured sections of Bandelier Tuff (Fig. 2). During progressive welding of ignimbrites, both the ash matrix and pumice lapilli deform (e.g., Ragan and Sheridan 1972). The pumice lapilli deform to form flattened ellipsoids having equatorial axes a and b and polar axis c. Ragan and Sheridan (1972) demonstrated, from measurements on cube shaped, oriented samples of Bishop Tuff and Aso 4 Tuff, that the equatorial axes (a and b) change equally as the vertical axis (c) shortens. Hence, when measured perpendicular to flattening direction, the height (c) and the length (a) of pumice lapilli fully describe the extent of deformation. Commonly, the ratio of axial length to height (a/c) is used to describe "flattened" lapilli (e.g., fiamme; Sheridan and Ragan 1976; Peterson 1979). However, to better describe deformation of pumice lapilli, we use the formula for oblateness:

$$1 - c/a \tag{4}$$

assuming that the equatorial axes of the ellipse (a and b) are equal.

We measured oblateness for 81 of the samples collected; some samples were too poor in pumice lapilli for oblateness to be measured accurately. Reported values of oblateness are the means of measurements on $\geq$20 pumice lapilli per sample. Each lapillus had to have a cross sectional area of at least 5 mm^2 and the average uncertainty (1σ) is ~7%.

During progressive welding ash shards align to form a fabric perpendicular to the direction of flattening (e.g., Smith 1960a). The orientations of individual glass shards (relative to horizontal) were determined through thin section analysis. Digital photomicrographs of oriented thin sections were taken for 19 samples from section SCC-1 and from samples of the Devine Canyon and Walcott Tuff. We traced a minimum of 100 particles from each photomicrograph using the pencil tool in Adobe Illustrator®. Near the edges of mineral grains (e.g., phenocrysts), shards commonly show enhanced alignment or deformation. Consequently, all fabric measurements were made well away (e.g., >1.5 times the diameter of the mineral grain) from the edges of any crystal. Using the Scion® (NIH) image analysis program, we fit an ellipse to each particle trace to best represent its orientation. The mean of each population is reported as the fabric angle: the angle of deviation from the horizontal. The most intensely welded (e.g., deformed and aligned) samples will have the lowest fabric angle. The average measurement uncertainty (1σ) is 3% and this was estimated by replicate analysis (e.g., five separate populations of particles) on a single thin section.

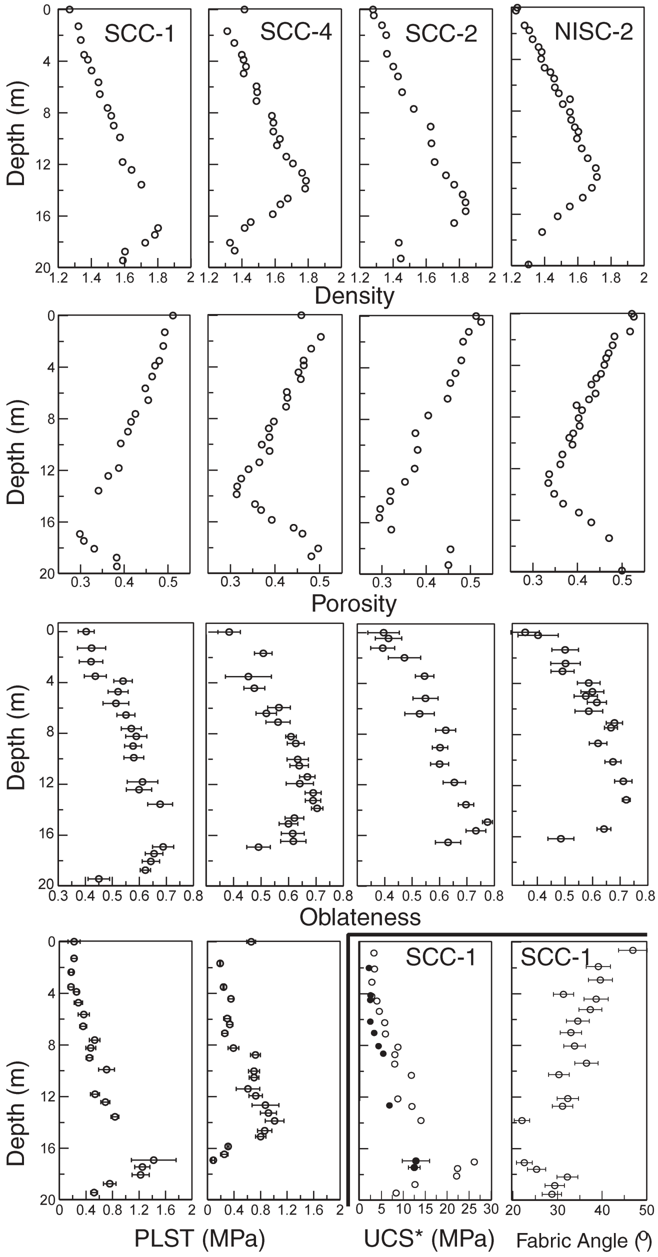

Fig. 2 Physical properties of samples from drill core sections from Unit 4 of the Tshirege member of the Bandelier Tuff are plotted as a function of depth (m), including: density (g/cm^3), fractional porosity, oblateness of pumice lapilli and point-load strength (PLST) (MPa). Samples are from four different drill hole sections (SCC-1, SCC-2, SCC-4 and NISC-2). All metrics vary systematically with depth and define maxima or minima between 13 and 17 m depth. Error bars denote 1σ uncertainties on PLST and oblateness measurements; corresponding 2σ uncertainties on density and porosity are smaller than symbols (see text for discussion of methods used to measure each metric). Panels separated by *solid black line* (*bottom right*) represent the additional physical properties uniaxial compressive strength (UCS) (measured-*solid circles* and predicted-*open circles*; Quane and Russell 2003) and fabric angle (in degrees) as a function of depth for core SCC-1

Metrics: strengths and weaknesses

To a first order, when plotted versus depth, all metrics show significant and systematic variation throughout the core and all appear to record similar variations in welding intensity. Furthermore, the metrics show similar patterns indicating a maximum in welding at ~17 m depth (Fig. 2). There are inherent strengths and weaknesses in the measurement and application of each metric. For example, density is relatively easy to measure and seems to provide a direct and accurate record of subtle changes in the welding process. Density, however, is affected by bulk composition of the magma or it can be modified by post-welding crystallization (e.g., lithophysae), and it varies with lithic and crystal contents. These issues lessen its utility for tracking welding intensity or making comparisons between deposits. Normalizing density (bulk density/matrix density) mitigates some of these effects and allows direct comparison between disparate pyroclastic deposits. Porosity tends not to be measured as precisely as density but has the same capacity to track subtle changes in welding intensity. Porosity is also affected by post-welding alteration (e.g., secondary porosity) but is less susceptible to the effects of crystal and lithic concentrations because both bulk and skeletal (or matrix) density are used in its calculation.

Rock strength offers a more indirect measure of welding intensity. *PLST* measurements can be made quickly in the laboratory or field on machined or irregular samples (e.g., Quane and Russell 2003), but tests are destructive and require a significant amount of material. *PLST* can be used to calculate *UCS*, which is a universally accepted metric of rock strength (e.g., Quane and Russell 2003). The uncertainties on rock strength measurements of welded pyroclastic deposits are relatively high compared to the other metrics (Fig. 2). Furthermore, pervasive secondary crystallization is likely to change the strength of welded pyroclastic materials.

Oblateness and fabric angle are direct measures of welding intensity and can be used to see through the effects of post-welding alteration for samples in which the vitroclastic textures remain. Oblateness is quite easily measured in the field or laboratory; however, some subtle changes in welding intensity are lost due to high variability of pumice flattening, perhaps due to differences in original porosity. It is however, a direct measure of strain accumulated by pumice lapilli (Fig. 2). Fabric angle measurements are relatively labor intensive and also do not seem to track subtle changes in welding as well as the other metrics (Fig. 2).

Covariation of metrics

The purpose of this section is to explore the relationships, or covariation, between the individual metrics used for welding intensity. Density has commonly been used for this purpose (e.g., Sheridan and Ragan 1976; Streck and Grunder 1995) and it has a low experimental uncertainty.

Table 2 Physical property data collected from the Devine Canyon. Walcott and Rattlesnake Tuffs including density (ρ), matrix density (ρ_m), porosity (ϕ), point load strength (*PLST*), uniaxial compressive strength (*UCS*), fabric angle (FA) and oblateness (OB)

Sample	ρ (g/cm^3)	ρ_m (g/cm^3)	2σ	ϕ	2σ	*PLST* (MPa)	1σ	*UCS* (MPa)	FA	1σ	OB	1σ
DVC 10–1	2.29	2.63	0.004	0.13	0.002	3.64	0.49	71.75	—	—	0.77	0.10
DVC 10–2	2.35	2.47	0.004	0.05	0.001	—	0.27	31.13	21.22	1.27	—	—
DVC 10–3	2.15	2.44	0.003	0.12	0.004	—	—	—	15.70	0.94	0.78	0.11
DVC 10–4	1.75	2.44	0.003	0.28	0.003	4.53	0.45	104.68	25.21	1.51	0.68	0.14
DVC 10–5	1.53	2.44	0.003	0.37	0.004	—	—	—	26.33	1.58	0.47	0.18
DVC 8–5	1.93	2.44	0.003	0.22	0.003	3.21	0.39	57.82	20.30	1.22	0.80	0.02
WT 85–3	1.66	2.41	0.003	0.31	0.004	2.07	0.27	28.34	40.46	2.43	—	—
WT 85–7	2.35	2.38	0.004	0.01	0.001	—	—	—	12.12	0.73	—	—
RT 1–2	1.89	2.38	0.002	0.21	0.002	—	—	—	—	—	0.62	0.23

We use normalized density as the standard for tracking welding intensity. The most densely welded samples of Bandelier Tuff in our dataset have a density of ~1.8 g/cm^3 and porosity of ~30%. We have supplemented the dataset with measurements on more densely welded material from the Devine Canyon Tuff (e.g., Greene 1973) and Walcott Tuff (e.g., Carr and Trimble 1963) and published values of ϕ, ρ and oblateness from four samples of the Bishop Tuff (Ragan and Sheridan 1972). Covariation between physical properties is illustrated by plotting each metric against normalized density (ρ_n) (Fig. 3). Each dataset (e.g., ρ_n vs. ϕ) is fit by least squares optimization to the generalized function:

$$y = a \cdot \rho_n^b + c \tag{5}$$

The form of this relationship is purely descriptive and not meant to reflect physical processes controlling variations between the metrics.

Porosity shows a near perfect 1:1 correlation with ρ_n (Fig. 3a) confirming that there is little unconnected porosity and indicating that welding in these samples is all accommodated by a loss in porosity.

The relationship between rock strength (*PLST* and *UCS*) and ρ_n is non-linear (Fig. 3b,c). For normalized densities up to ~0.65, rock strength shows a moderate and near linear increase but, above this value, rock strength increases dramatically for relatively small changes in ρ_n. At higher values of ρ_n rock strength is less precise and, as seen in previous studies (e.g., Price and Bauer 1985; Quane and Russell 2003), the measurements are only applicable to ρ_n up to ~0.9. Price and Bauer (1985) indicate a similar non-linear trend between *UCS* and ϕ for Yucca Mt. Tuff over a very large range in strength and ϕ (equivalent ρ_n from 0.35 to 0.9). It is apparent that after a certain amount of densification due to welding, the mechanical strength of pyroclastic flows drastically increases. This increase in strength likely results from the sintering of glassy particles as the contact area of individual ash particles increases with densification.

The relationship between ρ_n and both oblateness and fabric angle is non-linear (Fig. 3d,e). There is a rapid increase in oblateness and fabric angle during the first third of densification. Above values of ~0.6 ρ_n oblateness increases and fabric angle decreases only slightly and they are almost constant at ρ_n >0.9. The two properties show similar behavior, however, Sheridan and Ragan (1976) and Streck and Grunder (1995) suggest that, during welding, pumice lapilli deform more rapidly than the surrounding ash matrix. Pumice lapilli show a complete loss of porosity when the matrix still has ~10% porosity (Sheridan and Ragan 1976; Streck and Grunder 1995). This apparent decoupling of deformation processes during welding (e.g., lapilli vs. matrix) is likely a reflection of fundamental differences between the two components. Changes in fabric angle are presumably related to rotation of individual shards into the plane of the eutaxitic texture during progressive welding. In the initial stages of welding (e.g., high ϕ, low ρ_n) there is significant room for ash shards to rotate. However, as densification proceeds (e.g., ρ_n~0.7) there is little opportunity for rotation of ash shards to fill void space. At these high values of ρ_n loss of porosity in pumice lapilli appears to be more efficient.

Metrics of strain

The welding process largely reflects the accumulation of strain in pyroclastic materials and, therefore, metrics that track welding are also indicators of total strain (e.g., Ragan and Sheridan 1972; Sheridan and Ragan 1976; Kobberger and Schmincke 1999). The nature of strain induced by welding can be conceptualized by two end-member processes. Under plane strain, strain is induced by pure shear involving homogeneous flattening and requiring volume conservation. This requires flow in the plane of flattening. Conversely under volume strain, strain (e.g., flattening) is accumulated strictly by volume reduction (e.g., porosity loss). Most studies suggest that volume strain is most important during welding (e.g., Sheridan and Ragan 1976) until the onset of rheomorphic flow. If strain in pyroclastic deposits is accommodated entirely by porosity loss then ϕ and ρ_n serve as direct measurements of accumulated strain. Strain strictly accumulated from porosity loss can be calculated directly from porosity measurements $\epsilon(\phi)$ via:

$$\varepsilon(\phi) = \frac{\phi_o - \phi_1}{1 - \phi_1} \tag{6}$$

where ϕ_o is the initial porosity of the deposit (assumed here to be 60%; e.g., Sheridan and Ragan 1976) and ϕ_1 is

Fig. 3a–e Plots of normalized values of density (ρ_n) vs. measured values of **a**) porosity (ϕ), **b**) PLST, **c**) UCS, **d**) oblateness, and **e**) average fabric angle for all samples in this study. Suite includes samples from: the Bandelier Tuff (*circles*), Devine Canyon Tuff and Walcott Tuff (*triangles*) and Bishop Tuff (Sheridan and Ragan 1976; *diamonds*). *Solid lines* represent empirical functions $\left(y = a \cdot \rho_n^b + c\right)$ fitted to data; model values of a, b, c are shown in *upper left corner* (see text for details). Error bars are as discussed in Fig. 2

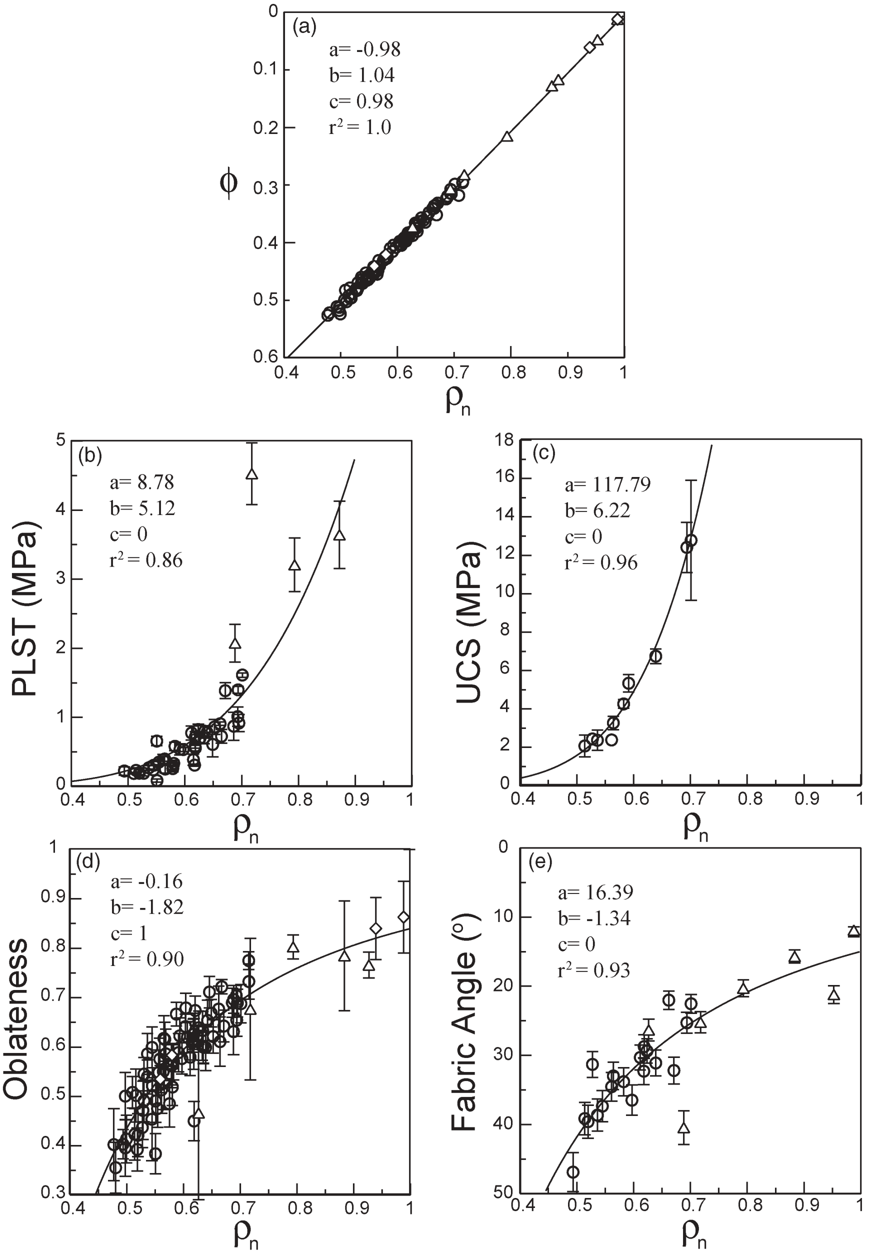

the porosity of the strained sample. A similar estimate of total strain based on ρ_n is given by:

$$\varepsilon(\rho_n) = \frac{\rho_{n_1} - \rho_{n_o}}{\rho_{n_1}} \tag{7}$$

where ρ_{no} is the initial normalized density of the deposit (assumed here to be 0.4; e.g., Sheridan and Ragan 1976) and ρ_{n1} is the normalized density of the strained sample. Lapilli oblateness is also a measure of strain in pyroclastic rocks but it tracks only the strain accommodated by collapsing of pumice lapilli whereas $\epsilon(\rho_n)$ and $\epsilon(\phi)$ track strain in the bulk deposit.

The calculated values of strain based on measurements of ρ_n, ϕ and oblateness are plotted for samples from section SCC-1 (Fig. 4a), other sections of Bandelier Tuff and supplementary samples (Fig. 4b). These data define a 1:1 relationship because the two physical properties (ρ_n and ϕ) are completely coupled (e.g., densification is driven only by porosity loss). Strain estimates based on oblateness, however, are greater than that of the bulk sample (Fig. 4c,d). Pumice lapilli that deform in a manner consistent with volume strain (viz., strain accommodated by porosity loss) will describe a linear relationship with zero intercept (solid lines; Fig. 4c,d). Conversely, if pumice lapilli deformation occurs on a constant volume basis (pure shear and no porosity loss) measurements of oblateness and $\epsilon(\rho_n)$ will have a non-linear relationship (dashed curves; Fig. 4c,d). The majority of oblateness and $\epsilon(\rho_n)$ data from SCC-1 exhibit a linear trend consistent with plane strain. However, unlike the ideal model, the observed trend does not pass through the origin probably

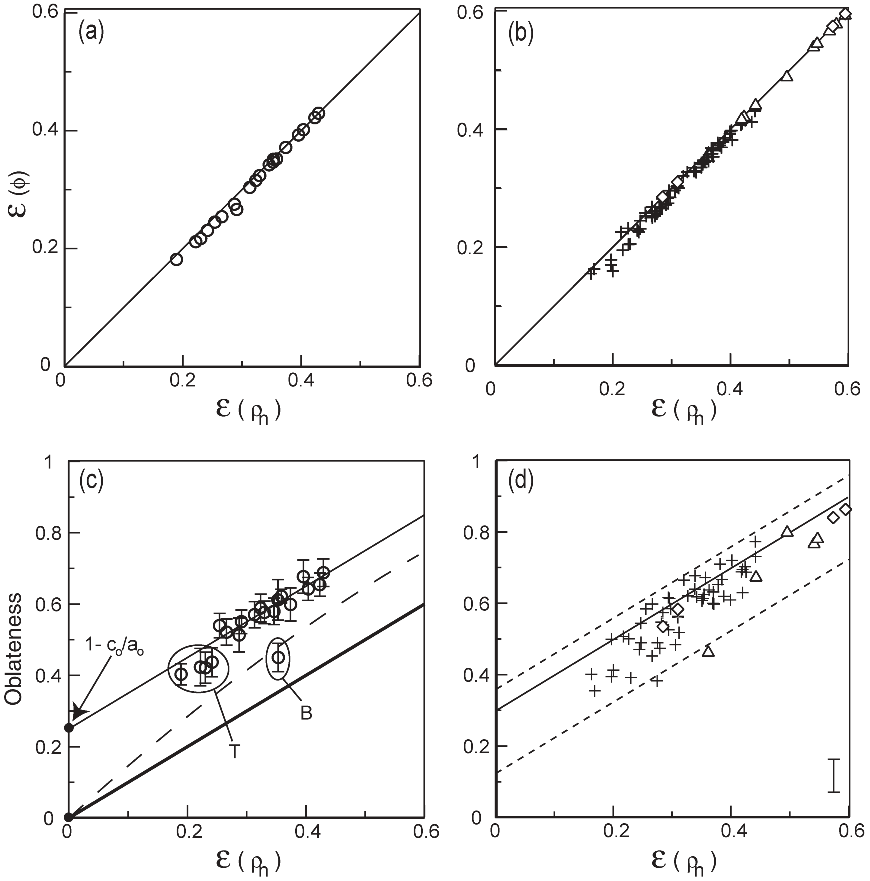

Fig. 4a–d Values of strain calculated from physical properties measured in this study. Strain calculated from porosity, $\epsilon(\phi)$ and density, $\epsilon(\rho)$ for **a**) SCC-1 samples (*open circles*) and **b**) all other samples in this study (SCC-2, SCC-4 and NISC-2 *crosses*; Devine Canyon Tuff and Walcott Tuff *triangles*; Bishop Tuff (Sheridan and Ragan 1976); *diamonds*). As expected, data fall very close to model line with unit slope and zero intercept (*solid line*). Oblateness of pumice fiamme vs. $\epsilon(\rho)$ for **c**) SCC-1 samples and **d**) all samples in this study (symbols same as in **a** and **b**). *Heavy solid line* in (**c**) denotes model relationships between oblateness and strain accumulated strictly from porosity loss. The Y-intercept of the different model lines (*solid* and *light*) represent the original oblateness of the pumice lapilli (e.g., 1-c_o/a_o). *Dashed curve* represents model relationship between oblateness and constant volume strain. Data from section SCC-1 are consistent with volume strain and an original oblateness value of 0.24. Where samples deviate from these model curves (top (T) and bottom (B) of sections), they record a greater loss in porosity than fiamme shape would suggest. **d**) Data from Bandelier Tuff samples (*crosses*) plot in the region defined by volume strain model lines with original oblateness values between 0.24±0.12 (*dashed lines*). Samples from the Bishop Tuff (Sheridan and Ragan 1976; *triangles*) plot near a model relationship for volume strain and an original oblateness of 0.32 (*solid line*)

because the pumice lapilli had an original oblateness prior to any welding deformation (e.g., Sheridan and Ragan 1976; Peterson 1979; Sparks and Wright 1979). The best approximation for data from SCC-1 is an original oblateness of 0.24 (Fig. 4a), a reasonable value when compared to observations made on measurements on nonwelded pumice lapilli from the Aso 4 and Bishop Tuffs (0.25 and 0.32 respectively; Sheridan and Ragan 1976). Still, 4 of 20 data points deviate and fall below the model line for homogenous strain with an original oblateness of 0.24. Such samples record a greater strain in terms of densification than suggested by measurements of oblateness. In every instance, these samples were collected from the top or bottom of the flow unit where cooling is fastest (e.g., Riehle 1973; Miller 1990; Riehle et al. 1995). In these locations, the processes of porosity loss and pumice lapilli flattening occur at substantially different timescales causing them to be decoupled. For example, early densification of the ashy matrix may result from largely mechanical compaction of particles that operates on a short timescale, relative to the viscous deformation driving the collapse of pumice lapilli (e.g., Sheridan and Ragan 1976). The "quenched" tops and bases of ignimbrites, therefore, record the points on the welding path where compaction processes dominate over processes limited by viscous flow.

The entire dataset is shown in Fig. 4d and, although there is considerably greater scatter, the pattern is similar. Nearly all data fit into the region covered by model lines allowing for an original oblateness of 0.24±0.12 (dashed lines; Fig. 4d). Again, samples from the Bandelier Tuff that fall below the model line are from the top and bottom of their respective flow units. The Bishop Tuff samples (diamonds; Sheridan and Ragan 1976) span a much larger welding range than the Bandelier Tuff samples (crosses). However, they follow a linear model trend consistent with an original oblateness of 0.32 (e.g., Sheridan and Ragan 1976; solid line), further suggesting that, within the uncertainty of the method used, most strain in the welding interval is accommodated by porosity loss.

Ranks of welding intensity

Here, we present a scheme for ranking the intensity of welding in pyroclastic deposits. Our classification scheme comprises six ranks (I-VI) that are defined by discrete ranges in physical property values and specific macroscopic or microscopic textural characteristics. The rank divisions are explicitly tied to previous schemes used to characterize welding intensity (e.g., Fig. 1; Smith 1960b; Smith and Bailey 1966; Sheridan and Ragan 1976; Peterson 1979; Streck and Grunder 1995; Wilson and Hildreth 2003). Specific petrographic characteristics used to define the individual ranks are listed in Table 3. Discrete ranges in physical properties for each rank were determined using the empirically derived covariation relationships between individual properties (Table 4). Field and thin section photographs are collated in Figs. 5 and 6, respectively, to illustrate the major structural changes used to define each rank.

Rank I consists of undeformed pumice lapilli in a loosely-packed, unconsolidated matrix (Figs. 5a and 6a). This rank describes the commonly used term “non-welded” (e.g., Smith 1960b; Peterson 1979; Streck and Grunder 1995; Wilson and Hildreth 2003) and comprises deposits with ρ_n values <0.60 (Table 4). Pumice lapilli and ash comprising Rank II remain undeformed (Table 4; Fig. 5b). However, some adhesion between clasts has occurred rendering the deposit coherent (e.g., Streck and Grunder 1995; Wilson and Hildreth 2003; Fig. 6b). The assigned range of ρ_n values (0.48–0.67) partly overlaps with that of Rank I and describes the commonly used terms “incipiently welded” (e.g., Peterson 1979; Streck and Grunder 1995) and “sintered” (Wilson and Hildreth 2003; Table 4). Rank III denotes the inception of deformation in the ash matrix and pumice lapilli (Figs. 5c and 6c). This rank is based on the divisions “partial welding” (Smith 1960b), “partially welded with pumice” (Streck and Grunder 1995) and “poorly welded” (Wilson and Hildreth 2003). The range of ρ_n is 0.67–0.76 (Table 4). Rank IV describes samples that have a clearly defined eutaxitic texture, however, the pumice lapilli show both moderate deformation as well as being collapsed to fiamme (Fig. 5d). Rank IV encompasses the term “moderately welded” (Wilson and Hildreth 2003) and is a subdivision of the term “partially welded with fiamme” (Streck and Grunder 1995) and describes deposits with ρ_n from 0.76–0.88 (Table 4). Samples having all pumice lapilli collapsed to fiamme (Fig. 5e) and a strongly foliated ash matrix (Fig. 6e) are assigned to Rank V. This rank is again a subdivision of the term “partially welded with fiamme” (Streck and Grunder 1995) and covers most of the term “densely welded” (e.g., Smith 1960b; Sheridan and Ragan 1976; Peterson 1979; Wilson and Hildreth 2003). The range of ρ_n for Rank V is 0.88–0.94. The most densely welded samples are placed into Rank VI. Rank VI comprises those samples that have been welded all the

Table 3 Petrographic characteristics used to define ranks of welding

Rank	*Ash matrix*	*Pumice lapilli*
I	Unconsolidated[1], noncoherent[4], loosely packed[2], little to no adhesion between shards[3]	Lack deformation[3], randomly oriented[2]
II	Coherent[4], some adhesion between shards[3], no coalescence of glassy material[3]	Randomly oriented[2], no deformation[3], no eutaxitic texture[4], fracture takes place around rather than through pumice[1]
III	Highly porous and soft[4], dull luster and hackly fracture[1], originally spherical bubble shards slightly ellipsoidal[3], some coalescence of glassy material[3]	Incipiently[1] or slightly[3] flattened[4]; fracture takes place through rather than around pumice[1]
IV	Relatively soft[4], moderately foliated[5] but individual shards only slightly deformed[3], contact area between shards increased[5] and clasts are moderatly adhered to one another[3]	Foliated into clear eutaxitic texture[4] with both moderately deformed pumice and fully collapsed fiamme present[3,5]
V	Shards strongly foliated[5], strongly adhered to one another[3] and moderately deformed[3]	Foliated into strong eutaxitic texture[4], collapsed to fiamme[3] that are obsidian-like although traces of former vesicles can be seen[1]
VI	Obsidian-like vitrophyre[1,3], shards are thoroughly collapsed[1,3], and completely adhered to one another[3]	Eutaxitic texture and obsidian-like fiamme are faintly visible[1] or difficult to detect[3]

[1] Smith 1960b; [2] Sheridan and Ragan 1972; [3] Streck and Grunder 1995; [4] Wilson and Hildreth 2003; [5] This study

Table 4 Range of physical properties associated with each welding rank

Rank	ϵ	ρ	ρ_n	ϕ	*PLST*	*UCS*	OB	FA
I	<0.31	<1.45	<0.60	>0.42	<0.59	<4.4	<0.58	>33.2
II	0.2–0.39	1.25–1.65	0.49–0.67	0.50–0.34	0.28–1.13	1.8–9.8	0.46–0.67	40.4–28.0
III	0.39–0.47	1.65–1.85	0.67–0.76	0.34–0.25	1.13–2.15	9.8–21.4	0.67–0.74	28.0–23.7
IV	0.47–0.52	1.85–2.15	0.76–0.88	0.25–0.13	2.15–4.6	21.4–53.2	0.74–0.8	23.7–19.5
V	0.52–0.57	2.15–2.3	0.88–0.94	0.13–0.07	4.6–6.4	53.2–80.2	0.8–0.82	19.5–17.8
VI	>0.57	>2.3	>0.94	<0.07	>6.4	>80.2	>0.82	<17.8

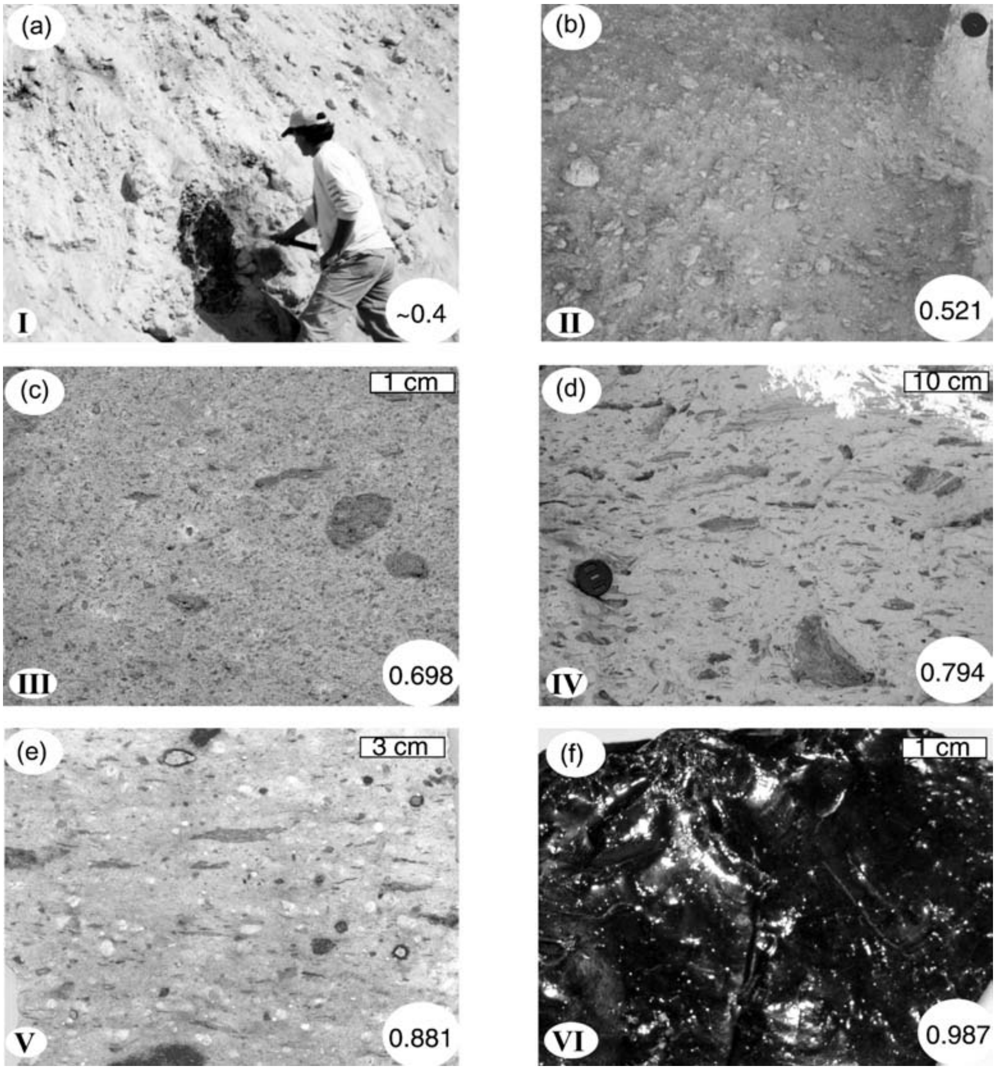

Fig. 5a–f Photographs showing macroscopic features used to delineate welding ranks (I-VI) in this study. Numbers in *bottom right corner* represent values of ρ_n measured on each sample (Tables 1 and 2). **a**) Pyroclastic flow deposit from Mt. Meager (Russell and Stasiuk 1997; rank I). The deposit is unconsolidated with randomly oriented pumice lapilli in a loose ash matrix. Deposit is easily disturbed by hand. **b**) Pyroclastic flow deposit within the Bandelier Tuff (rank II; sample SCC1–2). Pumice lapilli are randomly oriented in a matrix of consolidated ash (camera lens cap in *upper right hand corner* for scale). Deposit forms solid wall but individual pumice lapilli can be plucked with hammer and fractures go around pumice lapilli. **c**) Sample from the Bandelier Tuff (rank III; sample SCC2–14). Pumice lapilli are incipiently flattened and crudely aligned into eutaxitic texture. Fractures go through, rather than around, pumice lapilli. **d**) Outcrop of Rattlesnake Tuff (rank IV; sample RT1–2). Inclusions comprise both fiamme and moderately flattened pumice lapilli. **e**) Sample of Devine Canyon Tuff (rank V; sample DVC10–3). Pumice lapilli are fully collapsed to vitrophyric fiamme with virtually zero porosity. However, the matrix still retains some porosity. **f**) Sample from the Walcott Tuff (rank VI; sample WT85–7). Sample appears as massive vitrophyre with virtually zero porosity. However, individual shards can be seen with a hand lens on cut or broken faces

way to obsidian-like vitrophyre. Commonly, in this rank, the eutaxitic texture is difficult to detect in hand sample (e.g., Fig. 5f) and the glass shards are completely adhered to one another (Fig. 6f). This rank encompasses the term “densely welded” (Streck and Grunder 1995).

The ranking scheme described above reconciles the terminology used by previous workers to describe welding intensity (Fig. 1). In addition, it provides a number of criteria that can be used to classify the welding facies of individual outcrops because petrographic features (e.g., particle deformation) are explicitly tied to ranges of physical properties (e.g., ϕ). This ranking system will provide a consistent method of semi-quantitatively describing welding variations, thereby, replacing some of the more loosely defined and vague terms (e.g., moderately welded) used in the literature. The proposed ranking scheme also offers greater sensitivity or precision by expanding the welding scale to allow for six divisions (at a minimum); this will help capture the true nature of gradients in welding intensity recorded by different deposits.

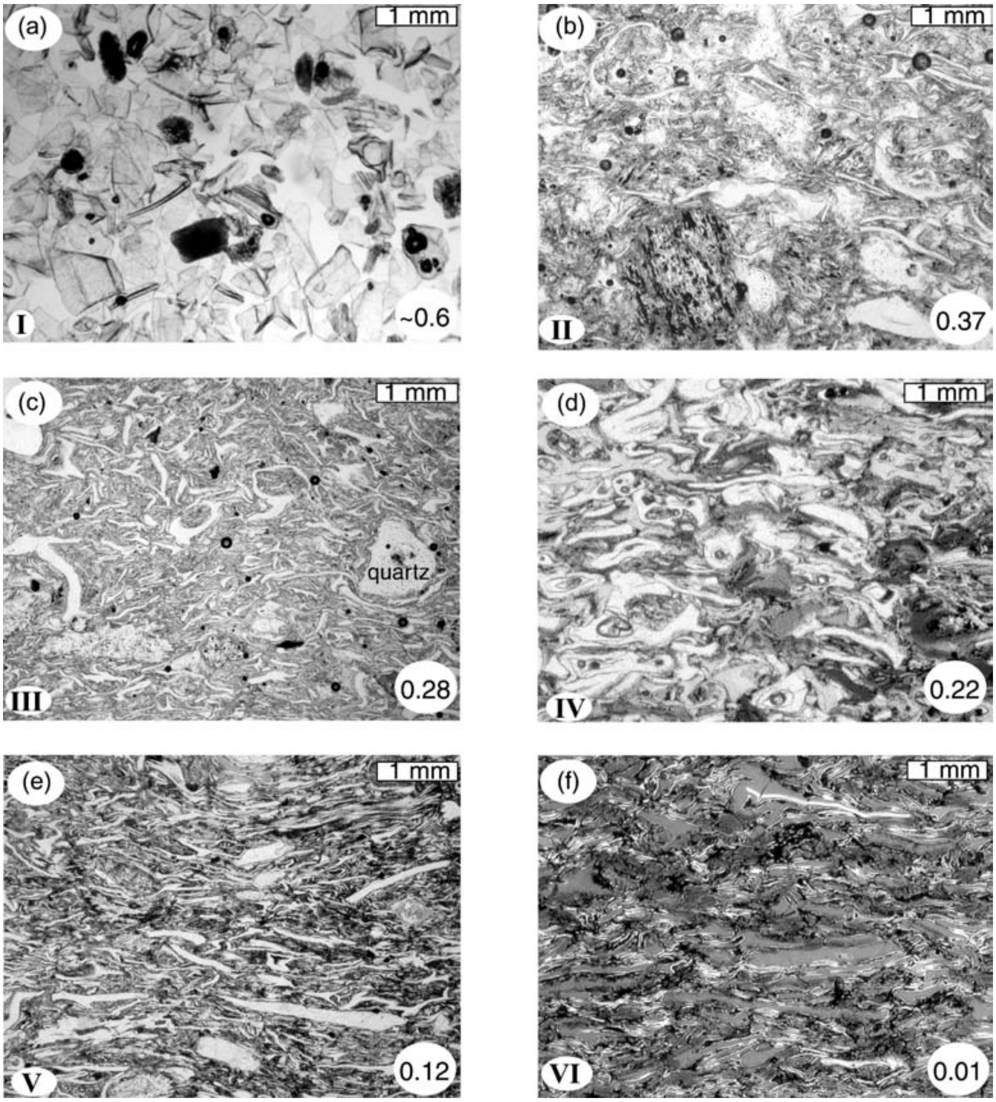

Fig. 6a–f Photomicrographs of petrographic characteristics used to delineate welding ranks (I-VI) in this study (all thin sections are oriented perpendicular to flattening direction). Numbers in *bottom right corner* represent values of ϕ measured on each sample (Tables 1 and 2). **a**) Unconsolidated glass shards from the Rattlesnake Tuff (rank I). Bubble and Y-shards are present, although most shards are tabular in form. None of the glass shards are deformed or adhered to one another. **b**) Sample of Devine Canyon Tuff (rank II; sample DVC10–5). Incipient adhesion of undeformed ash shards and pumice inclusions is present. **c**) Sample of Devine Canyon Tuff (rank III; sample DVC10–4). Original spherical bubble shards are slightly ellipsoidal. Ash shards are deformed around the edge of a quartz crystal inclusion. The remaining matrix is still randomly oriented. **d**) Sample of Devine Canyon Tuff (rank IV; sample DVC8–5). A weak but apparent foliation is developed in the ash shard matrix. **e**) Sample of Devine Canyon Tuff (rank V; sample DVC10–3). Strong foliation is apparent in the ash shard matrix. **f**) Sample of Walcott Tuff (rank VI; sample WT85–7). Ash shards are strongly flattened and adhered to one another. Further details of the petrographic characteristics used in this study can be found in text and Table 3

There are, however, caveats to this classification scheme. The ranks presented above are based on the properties of fresh pyroclastic rock samples that preserve their vitroclastic texture. In every case, the physical properties of the samples are a direct reflection of the welding process alone; the physical properties have not been significantly affected by secondary crystallization processes (e.g., lithophysae, sperulites; Streck and Grunder 1995). In nature, the effects of these processes can be pervasive and this potentially reduces the utility of our classification scheme. In such cases, one would have to rely almost exclusively on petrographic criteria for ranking welding intensity (e.g., Smith 1960b).

In this paper, we have treated welding intensity as equivalent to the strain accommodated by volume loss during compaction and flow of hot pyroclasts. The volume strain model describes well the welding that attends post emplacement compaction of pyroclastic materials that were deposited en masse (or very rapidly) or that cooled as a single unit (e.g., Smith 1960a; Sheridan and Ragan 1976; Wright and Walker 1981). However, there are situations where the strain manifest in pyroclastic deposits is not explicitly tied to porosity loss but instead represents coherent flow induced by pure or simple shear (constant volume) (e.g., rheomorphic ignimbrites; Schmincke and Swanson 1967; Walker and Swanson 1968; Elston and Smith 1970; Wolff and Wright 1981; Branney and Kokelaar 1992; Kobberger and Schmincke 1999; Sumner and Branney 2002). The indicators of strain (e.g., ρ, ϕ or oblateness) extracted from these types of deposits cannot be used in our classification scheme because the strain in these deposits records completely different deformation processes (e.g., non-coaxial pure or simple shear). Furthermore, the relationships between the metrics of strain (e.g., ϕ versus fabric) will be very different in these types of deposits than the covariations established here (e.g., Fig. 3). For example, rheomorphic ignimbrites will commonly show stretched and folded pumice lapilli with abnormally high length to height ratios in deposits that still have significant residual porosity (e.g., >25%; e.g., Wolff and Wright 1981; Streck and Grunder 1995; Kobberger and Schmincke 1999).

Application

Welded pyroclastic deposits are the final products of a complex sequence of volcanic processes involving eruption, flow and emplacement of pyroclastic materials. The welding process involves either syn or post-emplacement degassing, compaction, annealing and flow of glassy material (e.g., Smith 1960a; Ross and Smith 1961; Branney and Kokelaar 1992; Freundt 1998). Two of the most sought after and important pieces of information contained in a welded ignimbrite deposit are the thickness of the deposit at the time of deposition and the corresponding dense rock equivalent amount of erupted material. The method described below is most valid for ignimbrite deposits that have undergone post-emplacement deformation. For example, such deposits have deformed pumice lapilli oblateness values that are entirely consistent with flattening via porosity reduction alone (e.g., Fig. 4).

Ragan and Sheridan (1972) created a single welding profile for the Bishop Tuff on the basis of numerous density measurements on a composite section. We have converted their reported bulk densities into ρ_n and divided the section into welding ranks using the scheme outlined in Table 3 (Fig. 7a). Assuming all welding compaction is due to the removal of pore space, ρ_n values can be used as a proxy for strain in welded pyroclastic deposits. Strain is calculated for each sample for which density has been reported (Fig. 7a). The $\epsilon(\rho)$-depth data were fitted to a polynomial expression which was then integrated to provide estimates of average total strain as a function of depth (Fig. 7a). The average strain in the section increases down section to a maximum at ~130 m depth and then decreases slightly as the curve enters the less welded (Ranks I–III) base (Fig. 7a). The value at the base ($\epsilon(\rho)$= 0.429) represents the average total strain over the entire

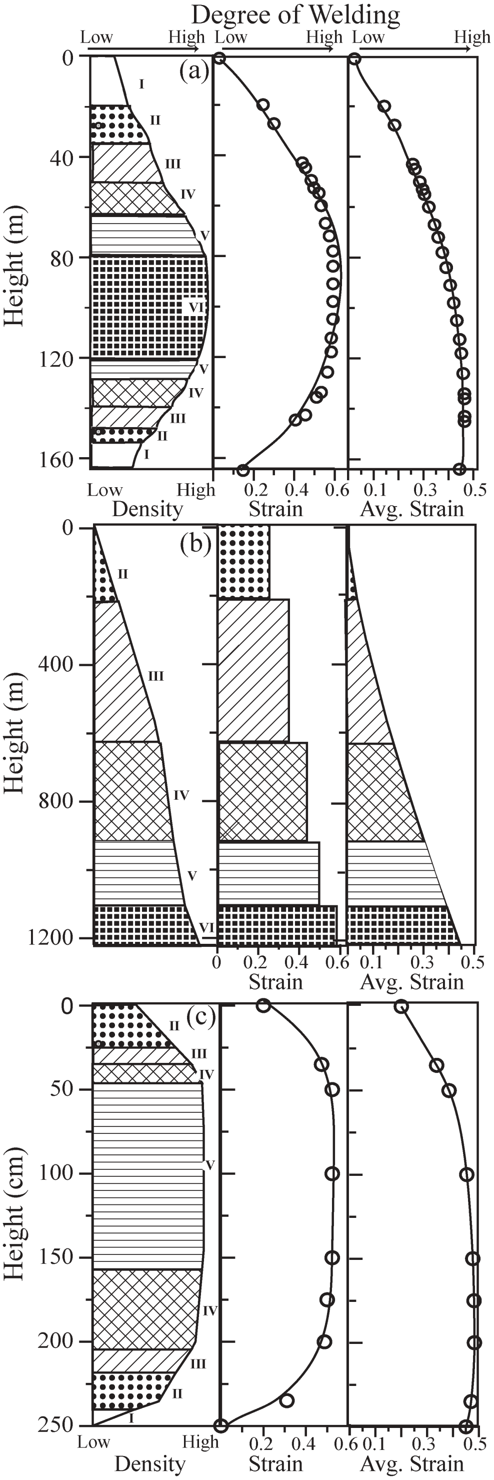

Fig. 7a–c Application of ranking system developed in this study to the (**a**) Bishop Tuff, (**b**) Bachelor Mt. Tuff and (**c**) Therasia welded air-fall tuff. *Left hand panels* in a–c are schematic representations of welding ranks. Welding rank divisions are based on normalized density values for **a** and **c** and petrographic features for **b**. *Middle panels* represent strain calculated from physical properties in **a** and **c** and average values for each rank in **b** (Table 4). *Right hand panels* represent average strain values with depth. Such diagrams allow for analysis of post-welding distribution of physical properties and are a basis for calculation of initial deposit thickness and distribution

section. This value can then be used to compute the original thickness of the section (L_o) from:

$$\varepsilon(\rho) = \frac{L_o - L_1}{L_o} \tag{8}$$

where L_1 is the current thickness (~165 m). Our estimate is 289 m, which is in close agreement to the original estimates of Sheridan and Ragan (1976).

This calculation of original thickness for a welded ignimbrite requires accurate measurements of both bulk and matrix density and an assumption of the average pre-welding porosity of the deposit. Significant amounts of post-welding crystallization (e.g., lithophysae) can change the bulk density and porosity of part or all of a welded section, rendering this method inaccurate. Therefore, an accurate prediction of original deposit thickness based on something other than density or porosity measurements could prove quite useful, especially in older, more altered welding facies.

Petrographic features are a viable alternative, tending to be more resilient to post-welding processes and remaining useful even in significantly altered rocks (e.g., McPhie et al. 1993). Here we calculate the pre-welding thickness of a multi-flow, simple cooling unit section of the Bachelor Mountain Tuff (Ratte' and Steven 1967) using the ranking system proposed in this study. Ratte' and Steven (1967) indicate that the Bachelor Mountain Tuff is pervasively altered by crystallization during cooling of the ash flow deposits, hence physical property measurements do not provide a reliable estimate of welding-induced changes. We have divided the ~1,220-m thick Bachelor Mountain Tuff stratigraphic column into ranks (Fig. 7b) using petrographic characteristics recovered from published photographs and photomicrographs and stratigraphic descriptions from a thick section of variably welded ignimbrite (Ratte' and Steven 1967). The average amount of strain recorded by each interval (ϵ_a) is calculated in the same fashion as above using the mid-value of ρ_n consistent with the assigned rank (Fig. 7b). The total strain achieved in the deposit (ϵ_T) is determined using the equation:

$$\varepsilon_T = \sum_{i=I}^{VI} h_r \cdot \varepsilon_a \tag{9}$$

where h_r is thickness (%) of material constituting each individual rank in the deposit and ϵ_a is the average strain for each rank division (Table 3; Fig. 7b). The total calculated strain is 0.455. Using the equation above we estimate an original thickness of 2,237 m for the Bachelor Mt. Tuff. This calculation demonstrates the usefulness of a ranking system comprising petrographic features and corresponding ranges of physical properties. This ranking system has the power to assign quantitative values to macroscopic and microscopic observations.

The ranking system proposed in this study is not limited to ash flow tuff deposits. Alternatively, any pyroclastic deposit that undergoes strictly volume strain can be ranked. Here, we apply our system to the Therasia welded air-fall tuff (Sparks and Wright 1979; Fig. 7c). The 250 cm thick welded air-fall tuff deposit shows a range of densities (Sparks and Wright 1979), which allows the unit to be divided into ranks I–V. The average total strain in the deposit (0.45) is higher than the value reported for the Bishop Tuff section despite the fact that the welded air-fall deposit does not reach welding rank VI. The pre-welding thickness of this air-fall deposit is calculated to be 455 cm.

Summary

We have explored the abilities of different physical properties to map variations in welding intensity using data collected from a single cooling unit of Bandelier Tuff. We have used these and supplementary data from more densely welded ignimbrite facies to develop a scheme for ranking or classifying the intensity of welding in pyroclastic deposits. Our ranking scheme comprises six divisions defined in terms of specific textural changes recording progressive deformation. We have also tied Ranks I-VI to characteristic ranges of physical properties (e.g., normalized density). The attributes of this proposed classification are two-fold. Firstly, it facilitates semi-quantitative comparisons of welding processes within different deposits or packages of pyroclastic material. Secondly, by coupling the petrographic-based ranking scheme to physical properties the individual ranks serve as approximate measures of strain.

Acknowledgements The authors would like to thank the staff of EES-6 at Los Alamos National Laboratory, especially Don Krier, for support and access to material of the Bandelier Tuff. We are indebted to Nick Austin for insightful discussions and help during laboratory measurements. This manuscript greatly benefited from very thorough and helpful reviews by Anita Grunder and Martin Streck. The Natural Sciences and Engineering Research Council of Canada (Discovery Grants program to JKR) and the Geological Society of America (Graduate Student Research Grant to SQ) supported this research.

References

Branney MJ, Kokelaar P (1992) A reappraisal of ignimbrite emplacement; progressive aggradation and changes from particulate to non-particulate flow during emplacement of high-grade ignimbrite. Bull Volcanol 54:504–520

Broxton DE, Reneau SL (1995) Stratigraphic nomenclature of the Bandelier tuff for the environmental restoration project at Los Alamos National Laboratory. Los Alamos Nat Lab Rep, LA-13010-MS, 21 pp

Carr W, Trimble DE (1963) Geology of the American Falls Quadrangle, Idaho. USGS Bull, pp G1-G44

Cas RAF, Wright JV (1987) Volcanic successions, modern and ancient; a geological approach to processes, products and successions. Allen and Unwin, London, pp 1–528

Elston WE, Smith EI (1970) Determination of flow direction of rhyolitic ash-flow tuffs from fluidal textures. Geol Soc Am Bull 81:3393–3406

Freundt A (1998) The formation of high-grade ignimbrites; I, Experiments on high- and low-concentration transport systems containing sticky particles. Bull Volcanol 59:414–435

Giordano D, Dingwell DB, Romano C (2000) Viscosity of a Teide phonolite in the welding interval. In: Marti J, Wolff JA (eds) The geology and geophysics of Tenerife. Elsevier, Amsterdam

Goff F (1995) Geologic map of technical area 21. In: Broxton DE, Eller PG (eds) Earth science investigations for environmental restoration–Los Alamos Laboratory Technical Area 21, Los Alamos National Laboratory report LA-12934-MS

Greene RC (1973) Petrology of the welded tuff of Devine Canyon, southeastern Oregon. USGS Prof Pap, USGS, Reston, VA, 26 pp

Hutchison CS (1974) Laboratory Handbook of Petrographic Techniques. Wiley, New York, 257 pp

Istok JD, Rautman CA, Flint LE, Flint AL (1994) Spatial variability in hydrologic properties of a volcanic tuff. Ground Water 32(5):751–760

Kobberger G, Schmincke HU (1999) Deposition of rheomorphic ignimbrite D (Mogan Formation) Gran Canaria, Canary Islands, Spain. Bull Volc 60:465–485

Krier D, Caporuscio F, Lavine A, Gardner J (1998) Stratigraphy and geologic structure at the SCC and NISC building sites, technical area 3, Los Alamos National Laboratory, New Mexico, Los Alamos National Laboratory technical report LA-13507-MS

McPhie J, Doyle M, Allen R (1993) Volcanic textures; a guide to the interpretation of textures in volcanic rocks. University of Tasmania, Centre for Ore Deposit and Exploration Studies, Launceston, TAS, 196 pp

Miller TF (1990) A numerical model of volatile behavior in nonwelded cooling pyroclastic deposits. J Geophys Res B 95: 19,349–19,364

Muller LD (1977) Density determination. In: Zussmann J (ed) Physical methods in determinative mineralogy. Academic Press, London, pp 663–673

Peterson DW (1979) Significance of the flattening of pumice fragments in ash-flow tuffs. In: Chapin CE, Elston WE (eds) Ash-flow tuffs. Special Paper, Geological Society of America, Boulder, CO, pp 195–204

Price RH, Bauer SJ (1985) Analysis of the elastic and strength properties of Yucca Mountain Tuff, Nevada. In: Ashworth E (ed) Research and engineering applications in rock masses. Proc Symp on Rock Mechanics. Balkema, Rotterdam, pp 89–96

Quane SL, Russell JK (2003) Rock strength as a metric of welding intensity in pyroclastic deposits. Eur J Min 15:855–864

Quane SL, Russell JK (2004) Welding: insights from high-temperature analogue experiments. J Volcanol Geotherm Res (In Press)

Quane SL, Russell JK, Kennedy LA (2004) A low-load, high-temperature deformation apparatus for volcanological studies. Am Min 89:873–877

Ragan DM, Sheridan MF (1972) Compaction of the Bishop Tuff, California. Geol Soc Am Bull 83(1):95–106

Ratte' JC, Steven TA (1967) Ash flows and related volcanic rocks associated with the Creede Caldera, San Juan Mountains, Colorado. USGS Prof Pap 524-H, H1-H58

Riehle JR (1973) Calculated Compaction Profiles of Rhyolitic Ash-Flow Tuffs. Geol Soc Am Bull 84(7):2193–2216

Riehle JR, Miller TF, Bailey RA (1995) Cooling, degassing and compaction of rhyolitic ash flow tuffs; a computational model. Bull Volcanol 57(5):319–336

Ross CS, Smith RL (1961) Ash-flow tuffs; their origin, geologic relations, and identification. USGS Prof Pap 366 Reston, VA, 81 pp

Russell JK, Stasiuk MV (1997) Characterization of volcanic deposits with ground penetrating radar. Bull Volcanol 58:515–527

Russell JK, Quane SL (2004) Rheology of welding: Inversion of field constraints. J Volcanol Geotherm Res (In Press)

Rust AC, Russell JK (2000) Detection of welding in pyroclastic flows with ground penetrating radar; insights from field and forward modeling data. J Volcan Geotherm Res 95(1–4):23–34

Rust AC, Russell JK, Knight RJ (1999) Dielectric constant as a predictor of porosity in dry volcanic rocks. J Volcanol Geotherm Res 91(1):79–96

Schmincke HU, Swanson DA (1967). Laminar viscous flowage structures in ash-flow tuffs from Gran Canaria, Canary islands. J Geol 75(6):641–664

Sheridan MF, Ragan DM (1976) Compaction of ash-flow tuffs. In: Chilingarian GV, Wolf KH (eds) Compaction of coarse-grained sediments, II. Elsevier, Amsterdam, pp 677–717

Smith RL (1960a) Ash flows. Geol Soc Am Bull 71(6):795–841

Smith RL (1960b) Zones and zonal variations in welded ash flows USGS Prof Pap 354-F, pp 149–159

Smith RL, Bailey RA (1966) The Bandelier Tuff; a study of ash-flow eruption cycles from zoned magma chambers. Bull Volcanol 29:83–103

Sparks RSJ (1976) Grain size variations in ignimbrites and implications for the transport of pyroclastic flows. Sedimentology 23:147–188

Sparks RSJ, Wright JV (1979) Welded air-fall tuffs. In: Chapin CE, Elston WE (eds) Ash-flow Tuffs. Geol Soc Am Spec Pap 180, pp 155–166

Streck MJ, Grunder AL (1995) Crystallization and welding variations in a widespread ignimbrite sheet; the Rattlesnake Tuff, eastern Oregon, USA. Bull Volcanol 57(3):151–169

Sumner JM, Branney MJ (2002) The emplacement history of a remarkable heterogeneous, chemically zoned, rheomorphic and locally lava-like ignimbrite: 'TL' on Gran Canaria. J Volcanol Geotherm Res 115(1–2):109–138

Vaniman D, Wohletz K (1990) Results of geological mapping/fractures studies, TA-55 area. Los Alamos National Laboratory Seismic Hazards Memo EES1-SH90–17

Vaniman K, Wohletz K (1991) Revisions to report EES1-SH90–17, Los Alamos National Laboratory Seismic Hazards Memo EES1-SH91–12

Walker GW, Swanson DA (1968) Laminar flowage in a Pliocene soda rhyolite ash-flow tuff, Lake and Harney counties, Oregon. Geological Survey Research 1968, Chap. B. USGS Prof Pap Reston, VA, pp B37-B47

Wilson CJN, Hildreth W (2003) Assembling an ignimbrite: mechanical and thermal building blocks in the Bishop Tuff, California. J Geol 111:653–670

Wolff JA, Wright JV (1981) Rheomorphism of welded tuffs. J Volcanol Geotherm Res 10(1–3):13–34

Wright JV, Walker GPL (1981) Eruption, transport and deposition of an ignimbrite: a case study from Mexico. J Volcanol Geotherm Res 9:111–131